

Flat band based delocalized-to-localized transitions in a non-Hermitian diamond chain

Hui Liu,¹ Zhanpeng Lu,¹ Xu Xia,^{2,*} and Zhihao Xu^{1,3,†}

¹*Institute of Theoretical Physics and State Key Laboratory of Quantum Optics and Quantum Optics Devices, Shanxi University, Taiyuan 030006, China*

²*Academy of Mathematics and System Sciences, Chinese Academy of Sciences, Beijing 100190, China*

³*Collaborative Innovation Center of Extreme Optics, Shanxi University, Taiyuan 030006, China*

(Dated: May 15, 2024)

In this paper, we investigate the influence of quasiperiodic perturbations on one-dimensional non-Hermitian diamond lattices with an artificial magnetic flux θ that possess flat bands. Our study shows that the symmetry of these perturbations and the magnetic flux θ play a pivotal role in shaping the localization properties of the system. When $\theta = 0$, the non-Hermitian lattice exhibits a single flat band in the crystalline case, and symmetric as well as antisymmetric perturbations can induce accurate mobility edges. In contrast, when $\theta = \pi$, the clean diamond lattice manifests three dispersionless bands referred to as an "all-band-flat" (ABF) structure, irrespective of the non-Hermitian parameter. The ABF structure restricts the transition from delocalized to localized states, as all states remain localized for any finite symmetric perturbation. Our numerical calculations further unveil that the ABF system subjected to antisymmetric perturbations exhibits multifractal-to-localized edges. Multifractal states are predominantly concentrated in the internal region of the spectrum. Additionally, we explore the case where θ lies within the range of $(0, \pi)$, revealing a diverse array of complex localization features.

PACS numbers: 72.80.Ng, 72.20.Ee, 72.15.Rn

Anderson localization is a fundamental quantum phenomenon in which quantum waves become localized due to disorder [1] in their environment. In a three-dimensional (3D) scenario with uncorrelated disorder, the system exhibits an energy-dependent transition from extended to localized eigenstates. This critical energy level, denoted as E_c , is known as the mobility edge. The mobility edge plays a crucial role in shaping the properties and behavior of the system, including its conductivity [2] and thermoelectric response [3]. In contrast to traditional Anderson models with uncorrelated disorder, where even a minuscule amount of disorder leads to complete localization in 1D and 2D cases, the 1D Aubry-André (AA) model with a quasiperiodic modulation demonstrates a metal-insulator transition at a finite value of the onsite potential's amplitude [4] without mobility edges. Recently, various generalized AA models have been devised [5–8], which can display exact mobility edges. Importantly, quasiperiodic systems can give rise to a third category of states known as multifractal states [9], which exhibit both extended and non-ergodic properties. Consequently, in addition to the mobility edge, a novel type of mobility edge between multifractal and localized states has been proposed [10, 11]. This concept holds significant importance in developing models with multifractal states.

On the other hand, localization can also be attained in the absence of disorder, particularly in certain translation-invariant systems with energy bands that lack dispersion, denoted as flat bands [12–19]. These flat

bands are characterized by having energy levels independent of the momentum, $E(k) = E$, resulting in a large-scale degeneracy at the energy E . This extensive degeneracy leads to the presence of compact localized states (CLSs) within the flat bands [19], where the eigenstates are confined to a finite number of sites [20, 21]. The incorporation of quasiperiodic modulations into certain flat band geometries [22, 23] can precisely engineer and tune mobility edges. Notably, when a small amount of quasiperiodic AA disorder is introduced to a compactly localized "all-band-flat" (ABF) diamond chain, the resulting eigenstates exhibit multifractality [24–26], and an exact transition from multifractal to localized states is observed.

In recent times, non-Hermitian systems have garnered significant attention in both experimental and theoretical domains. These systems exhibit remarkable properties that lack counterparts in Hermitian systems. Notable among these properties are the non-Hermitian skin effect [27–30], the breakdown of the bulk-boundary correspondence in certain nonreciprocal systems, and the sensitivity of the system's spectrum to boundary conditions. The interplay between non-Hermiticity and disorder has ignited a fresh perspective on localization characteristics [31–33]. The intriguing explorations in the realm of non-Hermitian disordered systems have spurred consideration of the non-Hermitian effect within the context of flat band models with quasiperiodic modulation. In this paper, we systematically study the impact of quasiperiodic modulation on a diamond lattice featuring flat bands with nonreciprocal hoppings. We find that the symmetry of the external perturbations and the synthetic magnetic flux parameter θ play a pivotal role in shaping the localization properties.

*Electronic address: xiayu14@mails.ucas.ac.cn

†Electronic address: xuzhihao@sxu.edu.cn

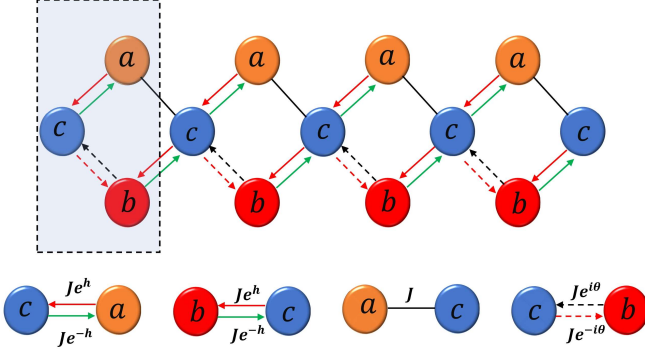


FIG. 1: (Color online) Schematic diagram of a non-Hermitian diamond lattice chain.

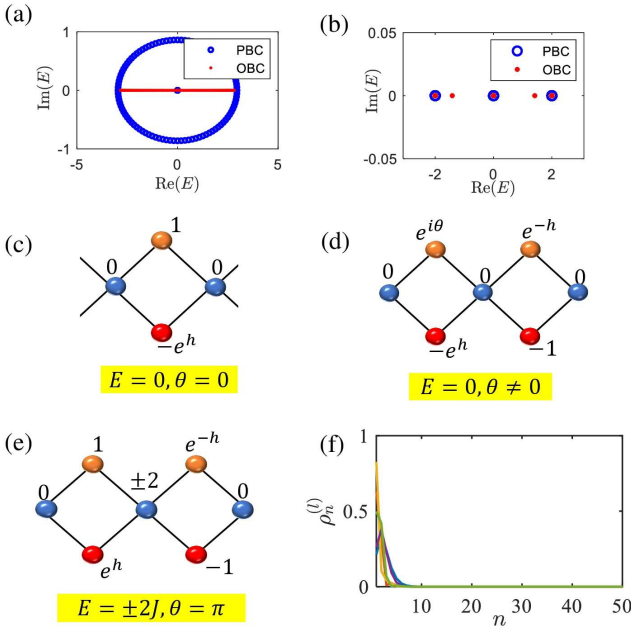


FIG. 2: (Color online) Crystalline Case: Energy spectra for (a) $\theta = 0$ and (b) $\theta = \pi$ under different boundary conditions. (c)-(e) The CLS occupations of the non-Hermitian diamond lattice in different flat bands for different θ . (f) Density distributions $\rho_n^{(l)}$ for six randomly selected eigenstates in dispersive bands with $\theta = 0$ under OBCs.

Model and method. We consider a non-Hermitian diamond chain with quasiperiodic perturbations. In the clean case as schematically illustrated in Fig. 1, there are three sublattices labeled by a , b , and c in each unit cell. We introduce nonreciprocal couplings marked by solid-line arrows between sublattices a and c in the same unit cell, and sublattices b and c in adjacent unit cells. Moreover, a synthetic magnetic flux θ is applied in each closed diamond loop via Peierls' substitution of the coupling constant between sublattices b and c in the same

unit cell. Consider the eigenvalue problem of a general-ized tight-binding model

$$E\psi_n = -J \left[\hat{V}\psi_n + \hat{T}_1\psi_{n-1} + \hat{T}_2\psi_{n+1} \right] + \hat{\epsilon}_n\psi_n, \quad (1)$$

with

$$\hat{V} = \begin{pmatrix} 0 & 0 & e^{-h} \\ 0 & 0 & e^{-i\theta} \\ e^h & e^{i\theta} & 0 \end{pmatrix}, \hat{T}_1 = \begin{pmatrix} 0 & 0 & 0 \\ 0 & 0 & 0 \\ 1 & e^{-h} & 0 \end{pmatrix}, \hat{T}_2 = \begin{pmatrix} 0 & 0 & 1 \\ 0 & 0 & e^h \\ 0 & 0 & 0 \end{pmatrix}, \quad (2)$$

where each component of the vector $\psi_n = (a_n, b_n, c_n)^T$ represents a site of a periodic lattice in the n -th unit cell, J is the coupling amplitude between adjacent sites with $J = 1$ being set as the unit of energy. h is a virtual gauge potential leading to nonreciprocal hoppings and non-Hermitian phenomena in the system. $\theta \in [0, \pi]$ is the synthetic magnetic flux, and the unit cell perturbation $\hat{\epsilon}_n$ of the Hamiltonian (1) is given by the diagonal square matrix $\hat{\epsilon}_n = \text{diag}(\epsilon_n^a, \epsilon_n^b, \epsilon_n^c)$.

In the crystalline case, where the on-site potential is set to be zero, the clean non-Hermitian model possesses three energy bands under periodic boundary conditions (PBCs) with the dispersion relations given by

$$E_0 = 0, \quad E_{\pm}(k) = \pm 2J \sqrt{1 + \cos \frac{\theta}{2} \cos \left(\frac{\theta}{2} + k - ih \right)}, \quad (3)$$

where $-\pi < k \leq \pi$ is the wave number. For $\theta \neq \pi$, there is only one flat band at energy E_0 , and the other two energy bands are k -dependent. We plot the energy spectra of $\theta = 0$ and π under PBCs marked by blue circles and open boundary conditions (OBCs) marked by red points in Fig. 2(a) and 2(b), respectively. For $\theta = 0$ under PBCs, all energies except E_0 are complex, whereas under OBCs, all energies become real. For $\theta = \pi$ under PBCs, the energy bands exhibit a remarkable dispersionless nature, showcasing energies of $E_0 = 0$ and $E_{\pm} = \pm 2J$. The energy spectrum remains real under OBCs for $\theta = \pi$. Like the Hermitian case, eigenmodes of our non-Hermitian model corresponding to those k -independent energies are CLSs whose amplitudes are nonzero only across a finite number of sites. Figure 2(c) illustrates the fundamental CLS for the $E = 0$ state with $\theta = 0$ in our cases, which occupies two sites and is localized in a single unit cell. When $\theta \neq 0$ and $E = 0$, the fundamental CLSs occupy four sites, shown in Fig. 2(d). The states of the additional flat bands at $E = \pm 2J$ for $\theta = \pi$ host five-site CLSs which excite one of the bottleneck sites seen in Fig. 2(e). Due to the existence of the nonreciprocal hoppings, the states in a dispersive band display the non-Hermitian skin effect under OBCs. To display the non-Hermitian skin effect, we calculate the l -th eigenstate's density distribution $\rho_n^{(l)} = \sum_{\beta \in \{a,b,c\}} |\psi_{n,\beta}^{(l)}|^2$, where $\psi_{n,\beta}^{(l)}$ represents the normalized probability amplitude of the β site in the n -th unit cell for the l -th eigenstate with the number of the

unit cell being N and the lattice size being $L = 3N$. In Fig. 2(f), we show $\rho_n^{(l)}$ for six randomly selected eigenstates in dispersive bands with $h = 0.6$, $N = 50$, and $\theta = 0$ under OBCs. According to Fig. 2(f), one can see that different states of dispersive bands show the non-Hermitian skin effect.

The effect of quasiperiodic AA perturbations is considered in the present work. The onsite perturbations $\{\epsilon_n^\beta\}$ for $\beta = \{a, b\}$ are defined as independent AA perturbations $\epsilon_n^\beta = \lambda_\beta \cos(2\pi\alpha n + \phi_\beta)$, where the parameters λ_β are positive real values controlling the quasiperiodic perturbative amplitude, ϕ_β is the phase shift, and α is an irrational number which is set to be the golden ratio $\alpha = (\sqrt{5} - 1)/2$. Without loss of generality, we set the a -leg phase to be zero ($\phi_a = 0$). Moreover, the a - and b -leg perturbation amplitudes are set to be equal to each other $\lambda_a = \lambda_b = \lambda \geq 0$. The c -leg potential is a uniform perturbation with the amplitude $\epsilon_n^c = K \in \mathbb{R}$.

We utilize a local coordinate transformation to the unit cells, which rotates these lattices into a Fano defect form [22, 34, 35]. The rotation for our non-Hermitian system is defined by a real matrix \hat{U}

$$\begin{pmatrix} p_n \\ f_n \\ c_n \end{pmatrix} = \hat{U} \begin{pmatrix} a_n \\ b_n \\ c_n \end{pmatrix}, \quad \hat{U} = \frac{1}{\sqrt{2}} \begin{pmatrix} 1 & e^{-h} & 0 \\ e^h & -1 & 0 \\ 0 & 0 & \sqrt{2} \end{pmatrix}, \quad (4)$$

with $\varphi_n = (p_n, f_n, c_n)^T$ being the rotated tight-binding representation of wave function of the n -th unit cell. Lastly, such local coordinate transformation also rotates the onsite perturbation. For the diamond chain, this gives

$$\epsilon_n^\pm = (\epsilon_n^a \pm \epsilon_n^b)/2. \quad (5)$$

From Eq.(5), the remarkable correlations between the a - and b -leg perturbations appear and will be an object of our studies in this work; namely

$$\begin{aligned} \text{Symmetric: } \phi_b = 0 & \Leftrightarrow \epsilon_n^- = 0, \\ \text{Antisymmetric: } \phi_b = \pi & \Leftrightarrow \epsilon_n^+ = 0. \end{aligned} \quad (6)$$

Since we have set the a -leg phase to be zeroed, according to Eq.(5), the correlations can be obtained from the b -leg phase, *i.e.*, $\phi_b = 0$ ($\phi_b = \pi$) for the symmetric (antisymmetric) case.

According to Eq.(4), the diamond lattice's Eq.(1) become

$$\begin{aligned} E p_n &= \epsilon_n^+ p_n + \epsilon_n^- e^{-h} f_n - \frac{1}{\sqrt{2}}(1 + e^{-i\theta})e^{-h} c_n - \sqrt{2}c_{n+1}, \\ E f_n &= \epsilon_n^+ f_n + \epsilon_n^- e^h p_n - \frac{1}{\sqrt{2}}(1 - e^{-i\theta})c_n, \\ (E - K)c_n &= -\frac{1}{\sqrt{2}} [(1 + e^{i\theta})e^h p_n + (1 - e^{i\theta})f_n] - \sqrt{2}p_{n-1}. \end{aligned} \quad (7)$$

Based on Eq.(7), we discuss different choices of θ and correlations between the a - and b -leg perturbations on the system's localization transitions.

To explore the localization properties of the eigenstates, one can calculate the l -th eigenstate's fractal dimension, which is defined as $D_2^{(l)} = -\ln I_2^{(l)}/\ln L$ with the inverse participation ratio (IPR) being $I_2^{(l)} = \sum_{n=1}^N \sum_{\beta \in \{a,b,c\}} |\psi_{n,\beta}^{(l)}|^4$. For a localized state, $I_2^{(l)} = O(1)$ in the thermodynamic limit and the corresponding $D_2^{(l)} \rightarrow 0$, while for an extended state, $I_2^{(l)}$ tends to zero in the large system size limit and the corresponding $D_2^{(l)} \rightarrow 1$. For a multifractal wave function, $D_2^{(l)} \in (0, 1)$ and the value of $I_2^{(l)}$ approaches zero in the $L \rightarrow \infty$ limit.

To further verify the existence of the multifractal region in our system, we apply the mean inverse participation ratio of a given region $\text{MIPR}(\sigma_{\tilde{\beta}}) = \frac{1}{N_{\sigma_{\tilde{\beta}}}} \sum_{l \in \{\sigma_{\tilde{\beta}}\}} I_2^{(l)}$, Where $\sigma_{\tilde{E}}$, $\sigma_{\tilde{M}}$, and $\sigma_{\tilde{L}}$ represent the spectra localized in the extended, multifractal, and localized regions, respectively, $\tilde{\beta} \in \{\tilde{E}, \tilde{M}, \tilde{L}\}$, and $N_{\sigma_{\tilde{\beta}}}$ is the total amount of eigenvalues belonging to $\sigma_{\tilde{\beta}}$. For a finite size system, we use the function $\text{MIPR}(\sigma_{\tilde{\beta}}) = \tilde{a} \times (1/L)^{\tilde{b}} + \tilde{c}$ for fitting and obtain the fitting parameters \tilde{a} , \tilde{b} , and \tilde{c} . For a perfectly localized region, $\text{MIPR}(\sigma_{\tilde{L}})$ maintains a constant that hardly changes with L . For a perfectly delocalized region, $\text{MIPR}(\sigma_{\tilde{E}})$ varies linearly with $1/L$ and $\tilde{c} \rightarrow 0$. When we consider the multifractal region, we can find that the fitting parameter $\tilde{b} \in (0, 1)$ with finite \tilde{a} , and the fitting parameter \tilde{c} approaches zero.

In addition, many extensions to the AA model have recently been applied to the non-Hermitian systems, where one has systematically examined the relationship between the real-complex transition in energy and the delocalization-localization transition [36]. In a class of AA models with nonreciprocal hoppings under PBCs, one discovered that delocalized states correspond to the complex and localized states to the real energies. Applying such properties, one can also detect the localization transitions of this class of non-Hermitian AA systems with nonreciprocal hoppings.

In the following paper, we utilize the exact diagonalization method to do our numerical calculations. We set $h = 0.6$ and $K = 0.7$ as a concrete example, and the PBCs are considered.

Localization features. We first consider the $\theta = 0$ cases for Eq.(7). It can be reduced into a tight-binding form by expressing the f_n and c_n variables through the p_n ones, which contains the p_n variables only:

$$\left[\frac{E(E - K)}{2} - 2 \right] p_n = (e^{-h} p_{n-1} + e^h p_{n+1}) + \tilde{\epsilon}_n^{(1)} p_n, \quad (8)$$

where the effective on-site potential

$$\tilde{\epsilon}_n^{(1)} = \frac{E - K}{2} \left[\epsilon_n^+ + \frac{(\epsilon_n^-)^2}{E - \epsilon_n^+} \right] \quad (9)$$

is a function of the two on-site energies of the diamond lattice $\epsilon_n^{a,b}$ and depends on the on-site energy K of the c -chain. Notice that regardless of the other system parameters, at the energy $E = K$ for $\theta = 0$, we have $p_n = f_n = 0$

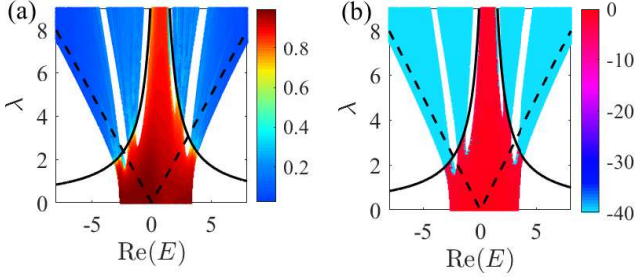


FIG. 3: (Color online) Symmetric Case with $\theta = 0$: (a) The real part of the spectrum $\sigma_{p,c}$ as a function of λ , where the color denotes the value of $D_2^{(l)}$. (b) $\ln |\text{Im}(E)|$ as a function of λ and $\text{Re}(E)$, where the color denotes the value of $\ln |\text{Im}(E)|$. The black solid lines represent the mobility edges given by Eq. (10). The spectrum σ_f is omitted, but its boundaries are indicated by black dashed lines. Here, $L = 600$.

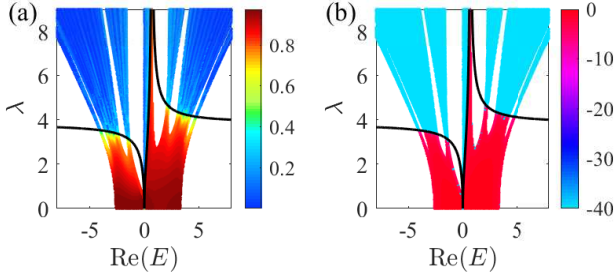


FIG. 4: (Color online) Antisymmetric Case with $\theta = 0$: (a) The real part of the spectrum as a function of λ , where the color denotes the value of $D_2^{(l)}$. (b) $\ln |\text{Im}(E)|$ as a function of λ and $\text{Re}(E)$, where the color denotes the value of $\ln |\text{Im}(E)|$. The black solid lines represent the mobility edges given by Eq. (11). Here, $L = 600$.

and $c_n = e^h c_{n+1}$, where the state's amplitudes reside on the c sites. Hence, an extended state exists under PBCs and a non-Hermitian skin state can be observed under OBCs at the energy $E = K$, independent of the modulation strength λ .

In the $\theta = 0$ case, the symmetric perturbation $\epsilon_n^- = 0$ can be obtained by setting $\phi_b = 0$. The f_n variables decouple from both the p_n and c_n variables, producing two independent spectra σ_f and $\sigma_{p,c}$. The σ_f keeps its compact feature with the energies given by $E = \epsilon_n^+$. Hence, all the states belonging to the spectrum σ_f are localized. In Fig. 3, we show the spectrum of the system with $\theta = 0$ and $\phi_b = 0$ as a function of λ . Due to the independence of the spectra σ_f and $\sigma_{p,c}$, we indicate the boundaries of the spectrum $\sigma_f = \{\epsilon_n^+\}$ by dashed lines in Fig. 3, which is equidistributed within the interval $[-\lambda, \lambda]$. To obtain the localization property of $\sigma_{p,c}$, we can obtain the tight-binding form only containing the p_n variables by choosing $\epsilon_n^- = 0$ in Eq. (8). The dispersive states p_n are described by a non-Hermitian AA chain with the

nonreciprocal hopping term. Referring to the discussion of the localization transition of the non-Hermitian AA model [37], we can obtain the mobility edges

$$\lambda_c = \left| \frac{4M}{E_c - K} \right|, \quad (10)$$

with $M = \max\{e^h, e^{-h}\}$. Figures 3(a) and 3(b) show the fractal dimension $D_2^{(l)}$ and the imaginary part of the spectrum $\sigma_{p,c} [\ln |\text{Im}(E)|]$ of different eigenstates belonging to the spectrum $\sigma_{p,c}$, respectively, as a function of the real part of the corresponding E and the modulation amplitude λ with $\theta = 0$, $\epsilon_n^- = 0$ and $L = 600$ under PBCs. The solid lines in Fig. 3 are the analytical solution of mobility edges. The real-complex transition in energy coincides with the localization transition shown in Fig. 3(b). One can see that our analytical result is in excellent agreement with the numerical results.

For the antisymmetric case $\epsilon_n^+ = 0$ obtained by $\phi_b = \pi$ for $\theta = 0$, all flat band states are expelled from their unperturbed energy position E_0 . Since $\epsilon_n^- \neq 0$, at the flat band energy E_0 , we can obtain $p_n = f_n = c_n = 0$. Therefore, only the trivial state $(p_n, f_n, c_n) = (0, 0, 0)$ satisfies Eq. (7) with $\theta = 0$ and $\phi_b = \pi$ at the flat band energy E_0 . In Figs. 4(a) and 4(b), we respectively plot the fractal dimension $D_2^{(l)}$ and $\ln |\text{Im}(E)|$ as the function of $\text{Re}(E)$ and λ in the case of antisymmetry and $\theta = 0$ with $L = 600$ under PBCs. In this case, mobility edges can be observed. The system can be described effectively by a non-Hermitian AA chain eigenequation with the nonreciprocal hoppings and the on-site modulation being $\lambda^2(E - K)/(4E) \cos(4\pi\alpha n)$. From Ref. [37], the analytic expression of the mobility edge is

$$\lambda_c = \sqrt{\left| \frac{8E_c M}{E_c - K} \right|}. \quad (11)$$

The analytic curve of the mobility edge Eq. (11) is plotted in Fig. 4 marked by the solid lines, displaying agreement with our numerical results.

For the $\theta = \pi$ cases for Eq. (7), we obtain a tight-binding form containing the p_n variables only:

$$\left[\frac{E(E - K)}{2} - 1 \right] p_n = \tilde{J}_n e^{-h} p_{n-1} + \tilde{J}_{n+1} e^h p_{n+1} + \tilde{\epsilon}_n^{(2)} p_n, \quad (12)$$

with

$$\tilde{\epsilon}_n^{(2)} = \frac{E - K}{2} \left[\epsilon_n^+ + \frac{(\epsilon_n^-)^2}{E - \epsilon_n^+ - \frac{2}{E-K}} + \frac{(\frac{2}{E-K})^2}{E - \epsilon_{n+1}^+ - \frac{2}{E-K}} \right], \quad (13)$$

and

$$\tilde{J}_n = \frac{\epsilon_n^-}{E - \epsilon_n^+ - \frac{2}{E-K}}. \quad (14)$$

The reduced topology displays a complex tight-binding form with the on-site perturbation term and the hopping terms being ϵ_n^+ , ϵ_n^- , and K dependent, which should present complex localization properties.

When we consider the symmetric case $\epsilon_n^- = 0$ for $\theta = \pi$, the intracell and intercell information can be written as the matrix form:

$$\hat{V}^{(1)} = \begin{pmatrix} 0 & 0 & 0 \\ 0 & 0 & \sqrt{2} \\ 0 & \sqrt{2} & 0 \end{pmatrix}, \quad \hat{T}^{(1)} = \begin{pmatrix} 0 & 0 & 0 \\ 0 & 0 & 0 \\ \sqrt{2} & 0 & 0 \end{pmatrix}. \quad (15)$$

And the lattice eigenvalue equation similar to Eq. (1) reads

$$E\varphi_n = - \left[\hat{V}^{(1)}\varphi_n + \hat{T}^{(1)}\varphi_{n-1} + \hat{T}^{(1)\dagger}\varphi_{n+1} \right] + \hat{\epsilon}_n^{(1)}\varphi_n, \quad (16)$$

with the on-site disorder matrix $\hat{\epsilon}_n^{(1)} = \text{diag}(\epsilon_n^+, \epsilon_n^+, K)$. A new unit cell can be identified considering the connected lattice sites $\tilde{\varphi}_n = (p_{n-1}, f_n, c_n)$, which affirms that the CLS of the disorder-free limit stays in one unit cell. The corresponding information on the intracell and the intercell reads

$$\hat{V}^{(2)} = \begin{pmatrix} 0 & 0 & \sqrt{2} \\ 0 & 0 & \sqrt{2} \\ \sqrt{2} & \sqrt{2} & 0 \end{pmatrix}, \quad \hat{T}^{(2)} = \begin{pmatrix} 0 & 0 & 0 \\ 0 & 0 & 0 \\ 0 & 0 & 0 \end{pmatrix}, \quad (17)$$

with the lattice eigenvalue equation

$$E\tilde{\varphi}_n = - \left[\hat{V}^{(2)}\tilde{\varphi}_n + \hat{T}^{(2)}\tilde{\varphi}_{n-1} + \hat{T}^{(2)\dagger}\tilde{\varphi}_{n+1} \right] + \hat{\epsilon}_n^{(2)}\tilde{\varphi}_n, \quad (18)$$

where $\hat{\epsilon}_n^{(2)} = \text{diag}(\epsilon_{n-1}^+, \epsilon_n^+, K)$. Observing the geometric information above, one can find that Eq.(18) displays the vanishing of the hopping between adjacent unit cells and the hopping term only exists within one unit cell. The extensive degeneracy is broken with the energy being modulation-dependent. With the help of the transformation, we display that the symmetric case with $\theta = \pi$ is made of three-site unit cells but with the absence of intercell hoppings, indicating the preservation of the CLSs even in the presence of the disorder. It means that all the states in such case are localized. This conclusion can be also got by setting $\epsilon_n^- = 0$ in Eq. (12), where the hopping term vanishes and it only exists the on-site modulation. Therefore, we can easily conclude that for a finite λ in the symmetric case with $\theta = \pi$, all the states are localized with non-degenerate energies.

For the antisymmetric case $\epsilon_n^+ = 0$ for $\theta = \pi$, when $E = K$, the tight-binding equation becomes

$$-\frac{2K}{\lambda}p_n = \cos(2\pi n\alpha)e^{-h}p_{n-1} + \cos(2\pi(n+1)\alpha)e^h p_{n+1}. \quad (19)$$

This model is equivalent to the non-Hermitian off-diagonal Harper model [36], where the $E = K$ modes remain multifractal for all the modulation amplitude. For the $E \neq K$ case, the tight-binding equation Eq. (12) can be given as:

$$\left[\frac{E^2(E-K) - 4E}{2\lambda} - \frac{\lambda(E-K)}{4} \right] p_n = \cos(2\pi n\alpha)e^{-h}p_{n-1} + \cos[2\pi\alpha(n+1)]e^h p_{n+1} + \frac{\lambda(E-K)}{4} \cos(4\pi n\alpha)p_n, \quad (20)$$

which is similar to a generalized Harper model with non-reciprocal hoppings [36], but its on-site perturbation frequency is twice that of the hoppings. According to Refs. [38, 39], it has not been allowed extended states that the mode described by Eq.(20). We plot the fractal dimension $D_2^{(l)}$ and $\ln|\text{Im}(E)|$ as the function of $\text{Re}(E)$ and λ in the case of antisymmetry and $\theta = \pi$ with $L = 600$ under PBCs, shown in Figs. 5(a) and 5(b), respectively. According to the numerical calculation, we can obtain the delocalized-to-localized edges

$$\lambda_c = \left| \frac{4M}{E_c - K} \right|, \quad (21)$$

which are plotted in Fig.5 marked by the solid lines. In the Hermitian limit with $h = 0$, Eq.(21) reduces to $\lambda_c = 4/|E_c - K|$, which has been studied numerically in Ref. [24]. One can see that in Fig. 5(a), the values of $D_2^{(l)}$ localized in the internal region between the two solid lines are around 0.55 to 0.7, indicating that the states in this region may be multifractal under PBCs.

To further determine the localization properties in this case, we consider the fractal dimensions $D_2^{(l)}$ for each eigenstate at different system sizes, which is shown in Fig. 6(a) with $\lambda = 5$ and $\theta = \pi$ under PBCs. In the finite-size case, the fractal dimensions of the states in the localized regions extrapolate to 0. In contrast, the fractal dimension's values of the internal region between two analytical edges shown by Eq.(21) with $\lambda = 5$ are away from 0 and 1 for different sizes, which implies that the states in this internal region are multifractal, and the analytical edges correspond to the multifractal-to-localized edges. Furthermore, we calculate $\text{MIPR}(\sigma_{\tilde{M}})$ as a function of $1/L$ for different L shown in Fig.6(b). When $\lambda = 1$, all the states are multifractal, and the corresponding fitting parameters of $\text{MIPR}(\sigma_{\tilde{M}})$ are $\tilde{a} \approx 1.27$, $\tilde{b} \approx 0.705$, and $\tilde{c} \rightarrow 0$, respectively. For the $\lambda = 5$ case, the multifractal-to-localized edges are at $E_{c1} \approx -0.75$ and $E_{c2} \approx 2.15$, and the corresponding fitting function is $\text{MIPR}_{\lambda=5}(\sigma_{\tilde{M}}) \approx 1.018L^{-0.699}$ with $\tilde{c} \rightarrow 0$. The multifractal-to-localized edges of $\lambda = 9$ are at $E_{c1} \approx -0.1$ and $E_{c2} \approx 1.5$. The fitting function is $\text{MIPR}_{\lambda=9}(\sigma_{\tilde{M}}) \approx$

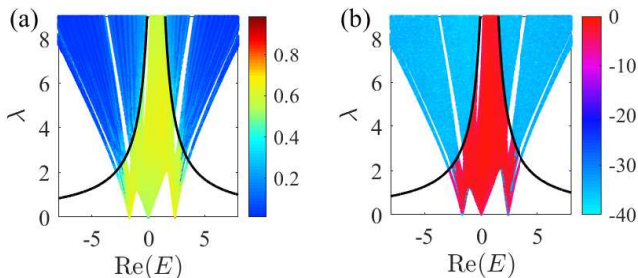


FIG. 5: (Color online) Antisymmetric Case with $\theta = \pi$: (a) The real part of the spectrum as a function of λ , where the color denotes the value of $D_2^{(l)}$. (b) $\ln |\text{Im}(E)|$ as a function of λ and $\text{Re}(E)$, where the color denotes the value of $\ln |\text{Im}(E)|$. The black solid lines represent the multifractal-to-localized edges given by Eq. (21). Here, $L = 600$.

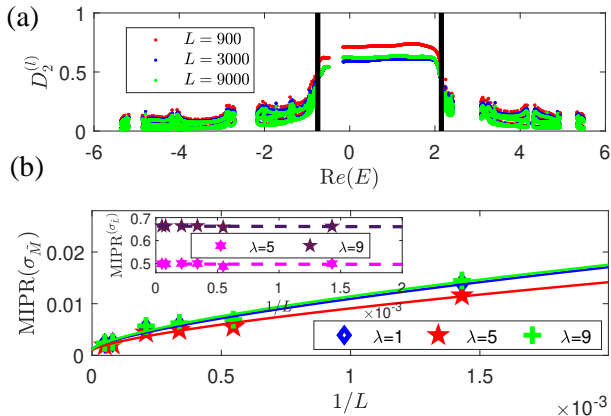


FIG. 6: (Color online) Antisymmetric Case with $\theta = \pi$: (a) $D_2^{(l)}$ for each eigenstate at different system sizes with $\lambda = 5$. (b) The scaling of $\text{MIPR}(\sigma_M)$ for different λ . The inset shows the scaling of $\text{MIPR}(\sigma_L)$ for different λ .

$1.061L^{-0.670}$ with $\tilde{c} \rightarrow 0$. According to the fitting parameters of the mean inverse participation ratios of the internal regions, we can further determine that the states in the internal regions are multifractal. We also show the scaling of $\text{MIPR}(\sigma_L)$ for $\lambda = 5$ and 9 in the inset of Fig. 6(b). Both cases display the L -independent behavior, and in the thermodynamic limit, $\text{MIPR}(\sigma_L)$ tend to finite values. Our results imply that the system has multifractal-to-localized edges for the $\theta = \pi$ and antisymmetric case, which can separate the multifractal states from the localized ones.

In the following, we consider when $\theta \in (0, \pi)$, the localization properties for both symmetric and antisymmetric cases. For the symmetric case $\epsilon_n^- = 0$, when $\theta = 0$, the system presents two independent spectra, σ_f and $\sigma_{p,c}$, where the σ_f keeps the localized properties and the $\sigma_{p,c}$ displays the mobility edges separating the extended states from the localized ones. Figures 7(a)-7(c) show

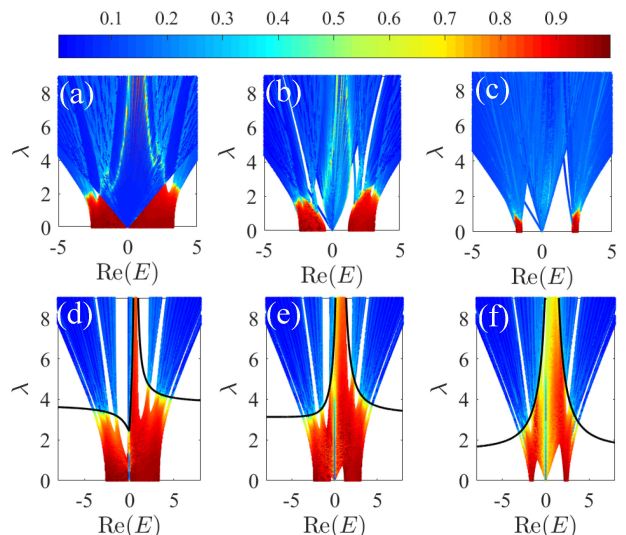


FIG. 7: (Color online) $D_2^{(l)}$ as a function of λ and $\text{Re}(E)$ with $L = 600$, where the color denotes the value of $D_2^{(l)}$. The top row corresponds to the symmetric cases, and the bottom row corresponds to the antisymmetric cases. From the left column to the right column, $\theta = 0.15\pi, 0.5\pi$, and 0.9π , respectively.

the fractal dimension $D_2^{(l)}$ of different eigenstates as a function of $\text{Re}(E)$ and the modulation amplitude λ for $\epsilon_n^- = 0$ with $\theta = 0.15\pi, 0.5\pi$, and 0.9π , respectively. In the small θ case, the spectra σ_f and $\sigma_{p,c}$ begin to couple together and display a weak coupling at the edges of the two spectra. With the increase of θ , in the small λ case, the proportion of the extended states gradually decreases in the band-edge regions. However, the band-center region gradually changes from a mixture regime with both extended and localized states to a multifractal regime to a localized regime. When $\theta \rightarrow \pi$, all the states become localized for an arbitrary finite λ . According to our numerical calculation, we can see that, in this case, the system displays a complex localization feature, and the existence of extended, localized, and multifractal regimes is detected. For the antisymmetric case $\epsilon_n^+ = 0$, we can obtain the exact extended-to-localized edges at $\theta = 0$, and when $\theta = \pi$, the multifractal-to-localized edges are given by Eq.(21). To obtain the localization information for an arbitrary θ , we plot $D_2^{(l)}$ as a function of $\text{Re}(E)$ and the modulation amplitude λ for $\epsilon_n^+ = 0$ with $\theta = 0.15\pi, 0.5\pi$, and 0.9π shown in Figs. 7(d)-7(f), respectively. We find that the delocalization-to-localization transition can be described by the equation

$$\lambda_c = 2\sqrt{\left|\frac{E_c M}{E_c - K}\right| \sqrt{2(1 + \cos \theta)} + \frac{2(1 - \cos \theta)M^2}{(E_c - K)^2}}, \quad (22)$$

which is plotted as the black solid lines in Figs. 7(d)-7(f). Despite the lack of analytical proof, the relation Eq.(22) works well in separating the delocalized and lo-

calized regimes for different θ . Eq.(22) can be considered an empirical combination of the corresponding analytical results under different limitations. When $\theta \rightarrow 0$, Eq.(22) reduces to Eq.(11), and for $\theta \rightarrow \pi$, Eq.(22) reduces to Eq.(21). Our results also suit the Hermitian cases with $h = 0$. Moreover, as seen in Figs.7(d)-7(e), the multifractal states are induced by increasing θ , and for an intermediate θ , it displays an extended and multifractal mixture in the band-center region.

Conclusion. This paper investigates the effects of a quasiperiodic AA perturbation on a one-dimensional non-Hermitian diamond lattice featuring flat bands. For $\theta = 0$, the system exhibits a single flat band in the crystalline limit. Symmetric and antisymmetric perturbations lead to the emergence of exact mobility edges. However, when $\theta = \pi$, the system becomes an ABF system without disorder. In this case, symmetric disorder per-

turbs the degeneracy completely, while the corresponding CLSs persist. In contrast, the application of antisymmetric modulation disrupts compact localization, giving rise to multifractal states for any finite modulation amplitude. We employ numerical calculations to derive the expression for the transition from multifractal to localized states, offering insights into this multifractal-to-localized edge. Furthermore, we explore cases where θ lies within the range $(0, \pi)$, revealing complex localization features within the system.

Acknowledgements. Z. Xu is supported by the NSFC (Grant No. 12375016), Fundamental Research Program of Shanxi Province (Grant No. 20210302123442), and Beijing National Laboratory for Condensed Matter Physics. X. Xia is supported by the NSFC (Grant No. 12301218). This work is also supported by NSF for Shanxi Province Grant No. 1331KSC.

-
- [1] Anderson P W 1958 *Phys. Rev.* **109** 1492
[2] Wang Y, Zhang L, Sun W *et al.* 2022 *Phys. Rev. B* **106** L140203
[3] Chiaracane C, Mitchison M T, Purkayastha A *et al.* 2020 *Phys. Rev. Res.* **2** 013093
[4] Aubry S and André G 1980 *Ann. Isr. Phys. Soc.* **3** 133
[5] Biddle J and Das Sarma S 2010 *Phys. Rev. Lett.* **104** 070601
[6] Wang Y, Xia X, Zhang L *et al.* 2020 *Phys. Rev. Lett.* **125** 196604
[7] Xu Z, Xia X, and Chen S 2022 *Sci. China: Phys. Mech. Astron.* **65** 227211
[8] Ganeshan S, Pixley J H, and Sarma S D 2015 *Phys. Rev. Lett.* **114** 146601
[9] Dai Q, Lu Z, and Xu Z 2023 *Phys. Rev. B* **108** 144207
[10] Liu T, Xia X, Longhi S *et al.* 2022 *SciPost Phys.* **12** 027
[11] Zhou X -C, Wang Y, Poon T -F J *et al.* 2023 *Phys. Rev. Lett.* **131** 176401
[12] Rhim J -W and Yang B -J 2021 *Adv. Phys.: X* **6** 1901606
[13] Talkington S and Claassen M 2022 *Phys. Rev. B* **106** L161109
[14] Morfonios C V, Röntgen M, Pyzh M *et al.* 2021 *Phys. Rev. B* **104** 035105
[15] Kuno Y, Mizoguchi T, and Hatsugai Y 2020 *Phys. Rev. B* **102** 241115(R).
[16] Zhang W, Addison Z, and Trivedi N 2021 *Phys. Rev. B* **104** 235202
[17] Ramezani H 2017 *Phys. Rev. A* **96** 011802(R)
[18] Sathe P and Roy R arXiv:2309.06487.
[19] Green D, Santos L, and Chamon C 2010 *Phys. Rev. B* **82** 075104
[20] Sutherland B 1986 *Phys. Rev. B* **34** 5208
[21] Aoki H, Ando M, and Matsumura H 1996 *Phys. Rev. B* **54** R17296(R)
[22] Bodyfelt J D, Leykam D, Danieli C *et al.* 2014 *Phys. Rev. Lett.* **113** 236403
[23] Danieli C, Bodyfelt J D, and Flach S 2015 *Phys. Rev. B* **91** 235134
[24] Ahmed A, Ramachandran A, Khaymovich I M *et al.* 2022 *Phys. Rev. B* **106** 205119
[25] Lee S, Andreanov A, and Flach S 2023 *Phys. Rev. B* **107** 014204
[26] Lee S, Flach S, and Andreanov A 2023 *Chaos* **33** 073125
[27] Yao S, Song F, and Wang Z 2018 *Phys. Rev. Lett.* **121** 136802
[28] Yao S and Wang Z 2018 *Phys. Rev. Lett.* **121** 086803
[29] Gong Z, Ashida Y, Kawabata K *et al.* 2018 *Phys. Rev. X* **8** 031079
[30] Xu Z, Xia X, and Chen S 2021 *Phys. Rev. B* **104** 224204
[31] Hatano N and Nelson D R 1996 *Phys. Rev. Lett.* **77** 570
[32] Hatano N and Nelson D R 1997 *Phys. Rev. B* **56** 8651
[33] Hatano N and Nelson D R 1998 *Phys. Rev. B* **58** 8384
[34] Miroshnichenko A E, Flach S, and Kivshar Y S 2010 *Rev. Mod. Phys.* **82** 2257
[35] Flach S, Leykam D, Bodyfelt J D *et al.* 2014 *Europhys. Lett.* **105** 30001
[36] Tang L-Z, Zhang G-Q, Zhang L-F *et al.* 2021 *Phys. Rev. A* **103** 033325
[37] Jiang H, Lang L -J, Yang C *et al.* 2019 *Phys. Rev. B* **100** 054301
[38] Dombrowski J 1978 *Proc. Amer. Math. Soc.* **69** 95
[39] Marx C A and Jitomirskaya S 2017 *Ergod. Th. Dynam. Sys.* **37** 2353